

Chapter 8

Three-body recombination

As greater densities are attained in ultracold atom experiments, their description in terms of two-body interactions is no longer sufficient. In fact, condensate densities limited by three-body inelastic collisions[153] have been achieved. It is conceivable that, in some regimes, an accurate theoretical treatment of mean-field energetics in a dense condensate will need to account for both two- and three-body elastic collisions. Probably the most dramatic three-body effect measured to date in a cold atom trap is the catastrophic loss of atoms from a Na condensate that was magnetically tuned to a Feshbach resonance[15]. It is believed that this loss was driven by three-body recombination, in which three free atoms coalesce allowing two to form a molecule while the third atom carries away most of the excess binding energy. Qualitatively, one might reason that the probability of three atoms colliding increases near a two-body resonance simply because the effective range of interaction between the atoms, characterized by the two-body scattering length a , becomes quite large. However, the Na experiment measured dramatic recombination rates even near $a \sim 0$, causing losses that severely limited the ability of that experiment to study the condensate near the resonance field value. It is not known whether this effect is unique to the Na atom or if it is instead an inevitable consequence of the three-body recombination physics.

Three-body recombination has been a largely neglected area of theoretical ultracold collision physics. A recent theoretical effort[154] predicted an a^4 scaling for the field-free recombination rate. However, the approximations used in that treatment are valid only in the limit of large positive a . Recombination of spin-polarized hydrogen[155, 156] was studied in the '80's and more recently in other alkali atoms[157], mostly within the confines of the Jastrow approximation. Those treatments based the recombination rates on a perturbative formulation that approximates the initial three-body wave function as a product of two-body wave functions. Using the Jastrow approximation, Moerdijk, *et al.*[157] obtained an a^2 scaling for the recombination rate which is at odds with the scaling proposed in Ref.[154]. In short, the physical processes that control three-body recombination have been poorly understood even at a qualitative level.

In this chapter, our first steps towards understanding the recombination

process are presented. In particular, we develop a quantitative method that can be used to calculate recombination rates that are stable as a function of both hyperradius and three-body continuum channels. Based on calculations using a wide range of two-body model potentials, we have been able to uncover universal systematics of the recombination physics. This work was first reported in Ref.[158]. The chapter is divided into two sections. In Section 8.1 the numerical method is developed. In Section 8.2 the results of our calculations are given and mechanisms for the recombination process are discussed.

8.1 Adiabatic hyperspherical representation

The formulation presented here has its origins in the work of Delves, who showed[159] that the three-body continuum can be represented by a countable set of channels in a hyperspherical representation. Most importantly the scattering matrix \underline{S} is symmetric and unitary in this representation. The hyperspherical coordinate method has been applied successfully to a number of diverse quantum mechanical three-body problems. (A review of these treatments can be found in Ref.[160]). The basic approach involves a coordinate transformation that first separates out the unimportant center-of-mass motion. The remaining six degrees of freedom are represented by three Euler angles and three internal coordinates, the hyperradius R and two hyperangles, θ and ϕ . It is unlikely that a resonance will occur over the range of collision energies available to cold magnetically trapped atoms. The Wigner threshold law leads to $K_3 \propto E^J$ near threshold therefore, it is sufficient to concentrate on collisions with total angular momentum $J = 0$. In this case the collisions are isotropic and the three-particle dynamics are described by a three-dimensional Schrödinger equation, which can be written in terms of hyperspherical coordinates.

There are numerous conventions for defining the hyperradial coordinates. In the case of identical particle scattering, the Smith and Whitten “democratic” coordinate system[161, 162] is the most useful. The definitions for the hyperangles (θ, ϕ) and hyperradius (R) are best developed in two stages, as shown in Ref.[163]. After separating out the center-of-mass motion, the remaining internal degrees of freedom are defined in terms of Jacobi coordinates ($\vec{\rho}_1, \vec{\rho}_2$). The relationship between the Jacobi coordinates and the space-fixed atom coordinates \vec{r}_i is given by[163]

$$\begin{aligned}\vec{\rho}_1 &= (\vec{r}_2 - \vec{r}_1)/d \\ \vec{\rho}_2 &= d \left[\vec{r}_3 - \frac{(m_1 \vec{r}_1 + m_2 \vec{r}_2)}{(m_1 + m_2)} \right]\end{aligned}\tag{8.1}$$

where m_i represents the atomic mass of atom i and the mass-weighting factor d is

given by

$$d^2 = \frac{(m_3/\mu)(m_1 + m_2)}{m_1 + m_2 + m_3} \quad (8.2)$$

$$\mu^2 = \frac{m_1 m_2 m_3}{m_1 + m_2 + m_3} .$$

The hyperradius and hyperangles are defined in terms of the Jacobi coordinates as follows[161]:

$$R^2 = \rho_1^2 + \rho_2^2 \quad (8.3)$$

and

$$\begin{aligned} (\rho_1)_{x'} &= R \cos \theta \cos \phi \quad , \quad (\rho_1)_{y'} = -R \sin \theta \sin \phi \\ (\rho_2)_{x'} &= R \cos \theta \sin \phi \quad , \quad (\rho_2)_{y'} = R \sin \theta \cos \phi . \end{aligned} \quad (8.4)$$

Here, (x', y') are Cartesian coordinates referred to the principal axes of the body-fixed system. Qualitatively, the hyperradius is a measure of the size of the three-body system. With these definitions, the hyperspherical coordinates have convenient symmetry properties that simplify the application of boundary conditions for identical particle scattering. In fact, for identical particle scattering it is only necessary to define the hyperangles over the range $0 \leq \theta \leq \pi/4$ and $0 \leq \phi \leq \pi/6$.

In general, the three-body interaction $V(R, \theta, \phi)$ can be approximated accurately by a sum of two-body interactions $v(r_{12}) + v(r_{23}) + v(r_{31})$. The first correction to this expression, the Axilrod-Teller term[32], has an R^{-9} dependence and should be unimportant for our problem. The three-body potentials used in this work are discussed in more detail in the next section. The two-body internuclear radii r_{ij} are defined in terms of the hyperradial coordinates by[163]

$$\begin{aligned} r_{12} &= 3^{-1/4} R [1 + \cos(2\theta) \cos(2\phi)] \\ r_{23} &= 3^{-1/4} R [1 + \cos(2\theta) \cos(2\phi + 2\pi/3)] \\ r_{31} &= 3^{-1/4} R [1 + \cos(2\theta) \cos(2\phi - 2\pi/3)] . \end{aligned} \quad (8.5)$$

The Schrödinger equation that describes the three particle dynamics is given in the hyperspherical representation by the following expression[163]:

$$\left\{ \frac{-\hbar^2}{2\mu} \left[\frac{1}{R^5} \frac{\partial}{\partial R} R^5 \frac{\partial}{\partial R} - \frac{\Lambda^2(\theta, \phi)}{R^2} \right] + V(R, \theta, \phi) \right\} \Psi = E\Psi . \quad (8.6)$$

The first derivative operator can be removed from this expression by introducing a

rescaled wave function $\psi = R^{5/2}\Psi$. The Schrödinger equation for ψ is then

$$\left\{ \frac{-\hbar^2}{2\mu} \left[\frac{\partial^2}{\partial R^2} - \frac{\Lambda^2 + 15/4}{R^2} \right] + V(R, \theta, \phi) \right\} \psi = E\psi. \quad (8.7)$$

Here, the grand angular momentum operator Λ^2 is given by the following expression:

$$\Lambda^2 = \frac{-1}{\sin 4\theta} \frac{\partial}{\partial \theta} \sin 4\theta \frac{\partial}{\partial \theta} - \frac{1}{\cos^2 2\theta} \frac{\partial^2}{\partial \phi^2}. \quad (8.8)$$

A standard approach to solve this three-dimensional Schrödinger equation begins by writing the three-body wave function as an adiabatic channel decomposition

$$\psi(R, \Omega, \chi) = \sum_{\nu=0}^{\infty} F_{\nu}(R) \Phi_{\nu}(R; \Omega, \chi). \quad (8.9)$$

Here Ω represents the two hyperangles and χ represents the spin degrees of freedom, while ν indexes the channel functions. The adiabatic channel functions $\Phi_{\nu}(R; \Omega, \chi)$, which vary smoothly in R except near avoided crossings, are eigenfunctions of the fixed- R hyperspherical Hamiltonian

$$\left[\frac{\hbar^2(\Lambda^2 + 15/4)}{2\mu} + V(R, \Omega) \right] \Phi_{\nu}(R; \Omega, \chi) = U_{\nu}(R) \Phi_{\nu}(R; \Omega, \chi). \quad (8.10)$$

The adiabatic potentials $U_{\nu}(R)$ form a set of effective potentials that can be used to gain qualitative insight into the particle dynamics. Further, insertion of the channel decomposition of $\psi(R, \Omega, \chi)$ into Eq. 8.7 leads a set of coupled one-dimensional equations

$$\left[\frac{-\hbar^2}{2\mu} \left(\frac{1}{R^2} \frac{d^2}{dR^2} + 2\frac{P}{R} \frac{d}{dR} + \frac{Q}{R^2} \right) + \underline{U} - \underline{E} \right] \underline{F} = 0. \quad (8.11)$$

Here, $P_{\mu\nu} = \langle \Phi_{\mu} | \frac{d}{dR} \Phi_{\nu} \rangle$ and $Q_{\mu\nu} = \langle \Phi_{\mu} | \frac{d^2}{dR^2} \Phi_{\nu} \rangle$ represent coupling matrices. In practice, only the $P_{\mu\nu}^2 = -\langle \frac{d}{dR} \Phi_{\mu} | \frac{d}{dR} \Phi_{\nu} \rangle$ component of $Q_{\mu\nu}$ (see Eq. B.2) is needed to solve the coupled equations, which can be added to the potential matrix to form $\underline{W} = \underline{U} - \frac{\hbar^2}{2\mu} \underline{P}^2$.

Once the symmetric matrix \underline{W} and antisymmetric matrix \underline{P} are determined, the coupled hyperradial equations can be solved using essentially the same approach that was presented in Chapter 3 for two-body scattering. The coupled equations (Eq. 8.11) are solved using the adiabatic FEM \underline{R} -matrix code described in Appendix B subject to $F_{\nu}(0) = 0$ boundary conditions. The scattering matrix is then derived from the \underline{R} -matrix solutions according to the procedure developed in Section 3.2. However, we do find it necessary to integrate out to surprisingly large $R \sim 10^5$ a.u.

before matching to energy-normalized channel functions. A code that calculates \underline{W} and \underline{P} by first expanding the angular coordinates in a B-splines basis[164] followed by a diagonalization of the Hamiltonian using banded iterative techniques[165] has been developed by Dr. B. Esry. In practice, we use this code to calculate \underline{W} and \underline{P} over the hyperradial range $0 \leq R < 8a$, where a is the two-body scattering length. Beyond, $R \sim 8a$ the matrix elements of \underline{W} and \underline{P} are smooth and can be fitted to an inverse polynomial series. We use the following series expansions to define the asymptotic values of these matrix elements[166]:

$$\begin{aligned}
 W_{\lambda,\lambda} &= \left[c_1 + \frac{c_2}{R^2} + \frac{c_3}{R^3} \right] \\
 W_{\lambda,\gamma'} &= \left[\frac{c_1}{R^2} + \frac{c_2}{R^3} + \frac{c_3}{R^4} \right] \\
 W_{\gamma,\gamma'} &= \left[\frac{c_1}{R^2} + \frac{c_2}{R^3} + \frac{c_3}{R^4} \right] \\
 P_{\lambda,\lambda'} &= \left[\frac{c_1}{R^1} + \frac{c_2}{R^2} + \frac{c_3}{R^3} \right] \\
 P_{\lambda,\gamma'} &= \left[\frac{c_1}{R^{5/2}} + \frac{c_2}{R^{7/2}} + \frac{c_3}{R^{9/2}} \right] \\
 P_{\gamma,\gamma'} &= \left[\frac{c_1}{R^2} + \frac{c_2}{R^3} + \frac{c_3}{R^4} \right] ,
 \end{aligned} \tag{8.12}$$

where λ, λ' label the recombination channels and γ, γ' index the three-body continuum channels. The coefficients c_i are determined by a least squares fit to matrix elements calculated with the B-splines code at large R . Tests indicate that the coefficients c_i are relatively insensitive to the range of R used in the fit, provided that it corresponds to hyperradii greater than $\sim 6a$.

The last step needed is to relate the scattering matrix to the recombination rate. A generalization of the two-body cross section derivation given in Section 2.1 has been developed[167], which defines the three-body recombination cross section for identical particle scattering in the following manner:

$$\sigma_3 = \frac{1152\pi^2}{k^5} |S_{A_2+A \leftarrow A+A+A}|^2 . \tag{8.13}$$

Here, $k = \sqrt{2\mu E/\hbar^2}$ is the hyperradial wavenumber in the incident three-body continuum channel. The large coefficient in Eq. 8.13 is a result of Bose-Einstein statistics and is a $(3!)^2$ -fold enhancement of the cross section compared to one that would be obtained for nonidentical particle scattering. The generalized cross section has dimensions $(length)^5$ as is expected for radial flux scattered in six dimensions. The cross section defined here follows the Mott and Massey[24] convention for identical particle scattering. That is, the cross section is defined as the ratio of scattered radial flux to the incident flux in one of the six permutations of the incident plane wave. As with two-body scattering, the event rate constant K_3 per atom triplet

is defined in terms of the cross section as

$$K_3 = \frac{\hbar k}{\mu} \sigma_3 . \quad (8.14)$$

Finally, the atom-loss rate is given by

$$L_3 = 3K_3/6 . \quad (8.15)$$

Here, the factor of three denotes the loss of both the diatom and the final state atom from the trap. The division by six comes from the fact that there are $N^3/6$ atom triples in a fixed volume. These formulae (equations 8.13, 8.14, and 8.15) were derived for collisions in a thermal gas and need to be divided by a factor of six to describe collisions in a condensate[168].

8.2 Recombination rates and mechanisms

The three-body interaction potential used is a sum of triplet Born-Oppenheimer two-body potentials. This choice is appropriate for collisions of doubly-polarized atoms. The major numerical challenge of a fully quantum mechanical approach to solving the recombination problem is the sheer multiplicity of two-body bound states. This is evident from Fig. 8.1, which shows the adiabatic hyperspherical potential curves for the collision of three doubly-polarized ^7Li atoms. Each bound state supported by the two-body interaction is represented by exactly one hyperspherical three-body potential that converges asymptotically to a dimer bound state. For doubly-polarized ^7Li , this amounts to 118 recombination channels and the number grows still larger for the heavier alkalis, with 1466 recombination channels available for doubly-polarized ^{87}Rb collisions.

However, it is physically plausible that the dominant pathways for recombination will involve vibrational states closest to threshold, particular those with low angular momentum l . In fact, previous studies[154, 157, 169] suggest that the two-body scattering length a ultimately controls ultracold recombination rates. Based on this assumption, we rescale the two-body triplet potentials by an overall scaling factor γ , where $0 \leq \gamma \leq 1$. This scheme allows us to reduce the total number of recombination channels, which alleviates many of the numerical complexities, while allowing us to control a . This premise is tested by treating two-body potentials that support different numbers of bound states but which generate the same scattering length. In addition, a number of calculations have been performed using a potential of the form $v(r_{12}) = D \operatorname{sech}^2(r_{12}/r_0)$, which was utilized in the three-body study of Ref.[169]. If the recombination rate is controlled by a , then the exact form of the short-range potential should not matter.

We have performed calculations with roughly 125 different two-body potentials, including a wide range of scattering lengths and different numbers of two-

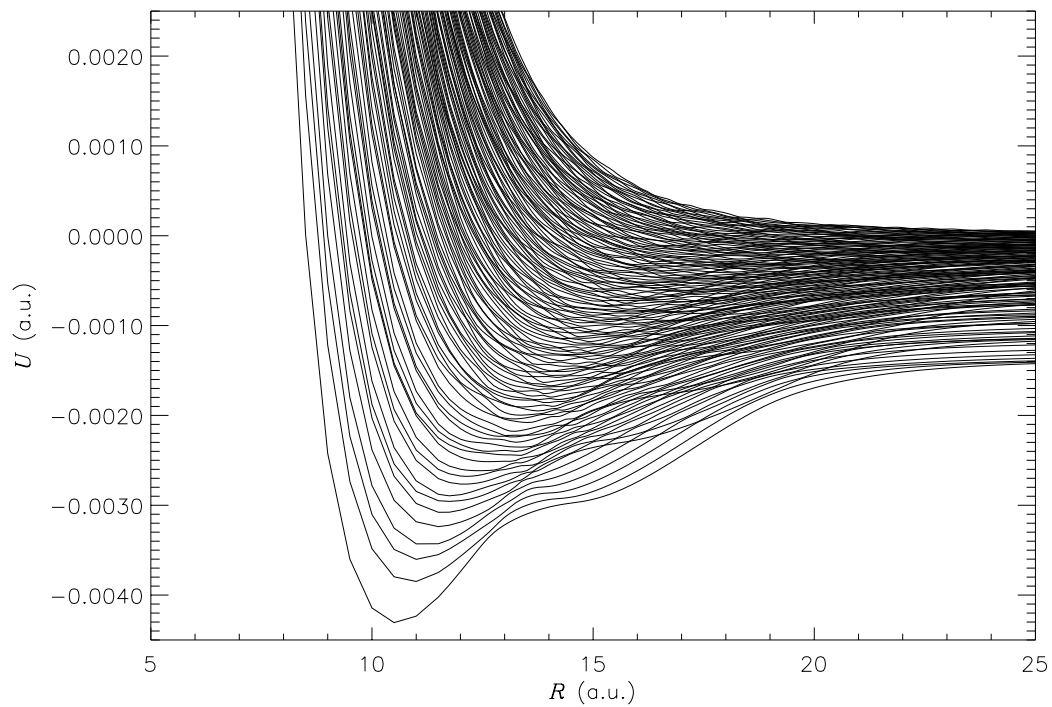


Figure 8.1: The $J=0$ hyperspherical potential curves for ${}^7\text{Li}$ are shown as a function of hyperradius R . These potential curves describe doubly-polarized collisions of three ${}^7\text{Li}$ atoms, i.e. all in the same $f_a = 2, m_{f_a} = 2$ spin state. All of the roughly 120 bound and continuum channels shown must be included in order to carry out a full calculation of the scattering matrix. Data courtesy of Dr. B. Esry.

body bound states. The potentials used include Na-Na, K-K, and Rb-Rb rescaled Born-Oppenheimer triplet potentials, and sech^2 potentials using $r_0=5$ and 15 a.u. Fig. 8.2 shows the resulting scattering length dependence of the “recombination length”. The recombination length is defined as

$$\rho_3 = \left(\frac{\mu}{\hbar} K_3 \right)^{1/4}. \quad (8.16)$$

Here, $\mu = m/\sqrt{3}$ is the three-body reduced mass. This definition is intended to present a quantity largely independent of the atomic properties other than the scattering length, and to reduce to a number roughly comparable to the scattering length in order of magnitude.

The most striking result of Fig. 8.2 is the manner in which the calculated recombination lengths cluster along a single curve. This implies that the recombination rates are in fact predominantly controlled by the two-body scattering length. In addition, Fig. 8.2 shows two additional features of the recombination process that had not appeared before in the literature. Specifically, an interference minimum occurs near $a \approx 290$ a.u. and a shape resonance occurs near $a \approx -175$ a.u. These features can be explained qualitatively by the two following mechanisms.

Recombination for positive scattering lengths is controlled primarily by a distant avoided crossing between the three-body entrance channel and the highest s -wave recombination channel that occurs near $R_{\text{peak}} \approx 3a$. Figure 8.3(a) shows the hyperspherical potential curves for the sech^2 two-body potential scaled to give $a = 100$ a.u. but with only a single s -wave bound state. In this case the hyperspherical potentials are very simple and their main features are consistent with Refs.[169, 170]. Figure 8.3(a) also shows the crossing near $R_{\text{peak}} \approx 3a$, as a peak in the dimensionless coupling strength parameter, $P^2/\mu\Delta U$. The approximate hyperradial peak position of $P^2/\mu\Delta U$ is plotted in Fig. 8.4 for a number of rescaled alkali potentials. The position of the crossing is consistent for the Rb-Rb and K-K rescaled potentials but approaches $R_{\text{peak}} \approx 4a$ for the large positive Na scattering lengths. It is not yet understood whether this deviation from the “nominal” behavior of the crossing position is an isolated occurrence.

The suppression of the recombination rates near $a \approx 290$ a.u. is analogous to that of the ^{87}Rb spin exchange rates discussed in Section 5.1. Namely, two competing pathways interfere destructively, which effectively “turns off” the flux exiting along the inelastic path. One minor difference between these two cases of so-called “Stückelberg oscillations” is that here the kinetic energy in the entrance channel is negative at the crossing. This case has been treated by Nakamura[171] who calls this process “nonadiabatic tunneling”. The scattering probability for recombination

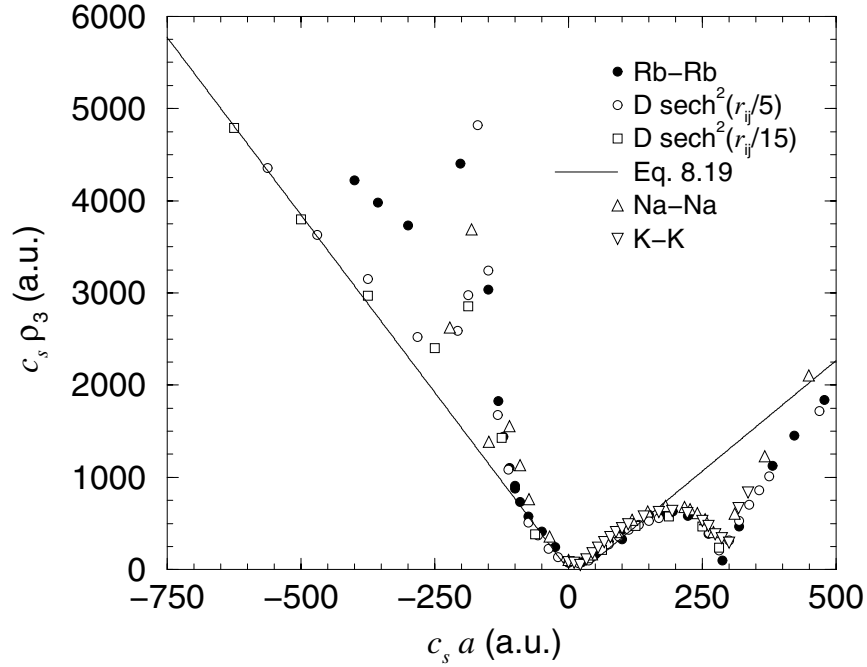


Figure 8.2: Numerically calculated recombination lengths for a wide range of two-body potentials, which are discussed in the text. We find that each set of two-body potentials has a characteristic length scale, labeled r_0 . In the case of the sech^2 potentials, r_0 is part of the definition of the potential, i.e. $v(r_{12}) = D \text{sech}^2(r_{12}/r_0)$, $r_0 = 5$ and 15 used here. The value of r_0 for the alkali potentials is determined “empirically” from the calculated position of the interference minimum and a zero of the phase factor $\sin^2[\ln(3a/2r_0)]$. (The phase factor is discussed in the text.) We find $r_0(\text{Rb}) = 18.8$, $r_0(\text{K}) = 16.8$, and $r_0(\text{Na}) = 12.4$ (in a.u.). The dimensionless scale factor is set to $c_s = r_0(\text{Rb})/r_0(V_i)$, i.e. $c_s = 1$ for the Rb potentials. Using this rescaling, each set of potentials produces an interference minimum near $c_s a \approx 290$ a.u. and a shape resonance near $c_s a \approx 175$ a.u. The solid line is the analytical formula given in Eq. 8.19 with the \sin^2 phase factor set equal to $\frac{1}{2}$. These calculations were performed at $E = 1 \mu\text{K}$, except for the range $a \leq -300$ a.u., where an energy of $0.1 \mu\text{K}$ was used in order to reach the ultracold limit.

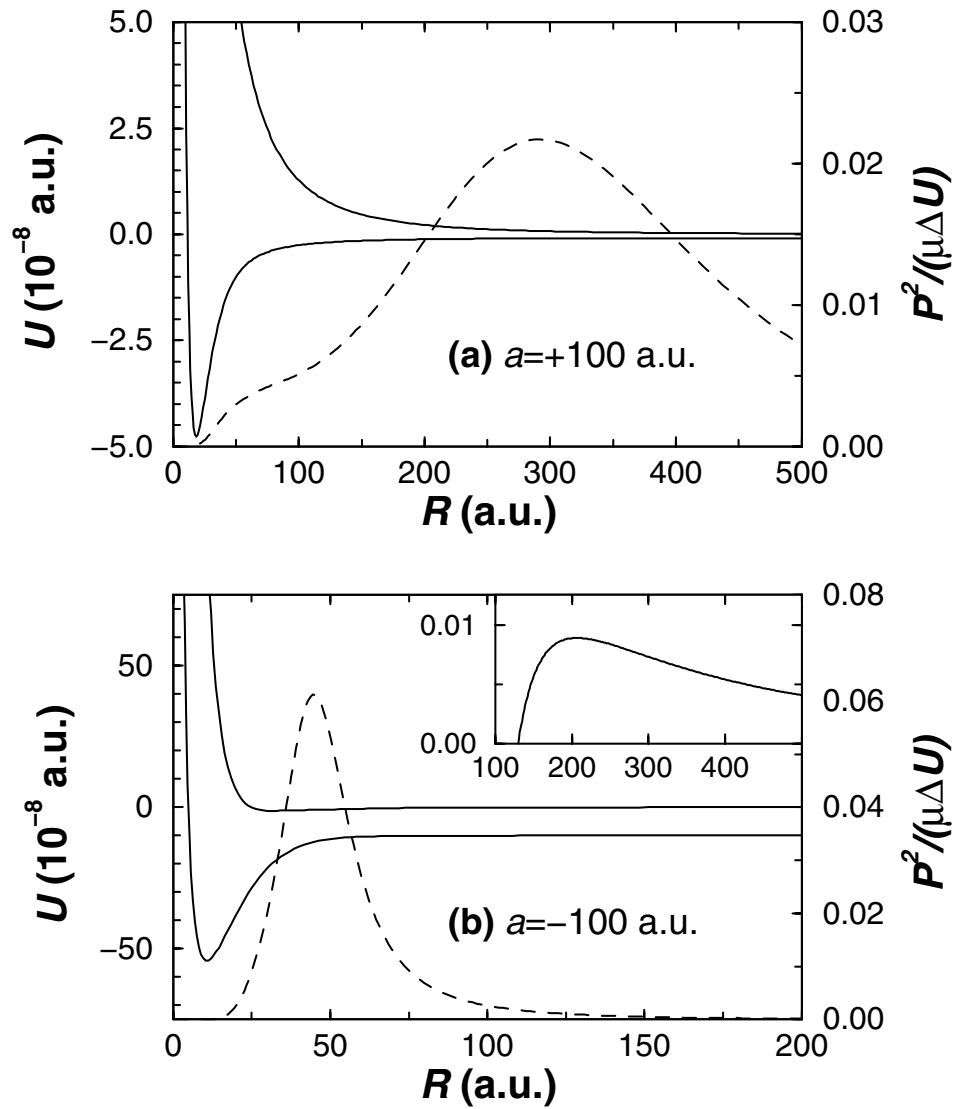


Figure 8.3: Different qualitative mechanisms control ultracold recombination at $a > 0$ (a) and $a < 0$ (b), as is clear from the lowest two adiabatic hyperspherical potential curves (solid line) depicted along with their nonadiabatic coupling strength (dashed line). We define a dimensionless measure of the nonadiabatic coupling strength in terms of the squared first derivative coupling matrix element $P_{12}^2(R)$, the difference in the adiabatic hyperspherical potential curves $\Delta U(R)$, and the reduced mass μ . These were calculated using the sech^2 two-body potential ($r_0 = 15$ a.u.) discussed in the text, for the simplest situation of a single two-body s -wave bound state. The basic nature of these potentials remains the same even as the number of two-body bound states is increased. The inset of (b) shows the potential barrier in the three-body entrance channel discussed in the text.

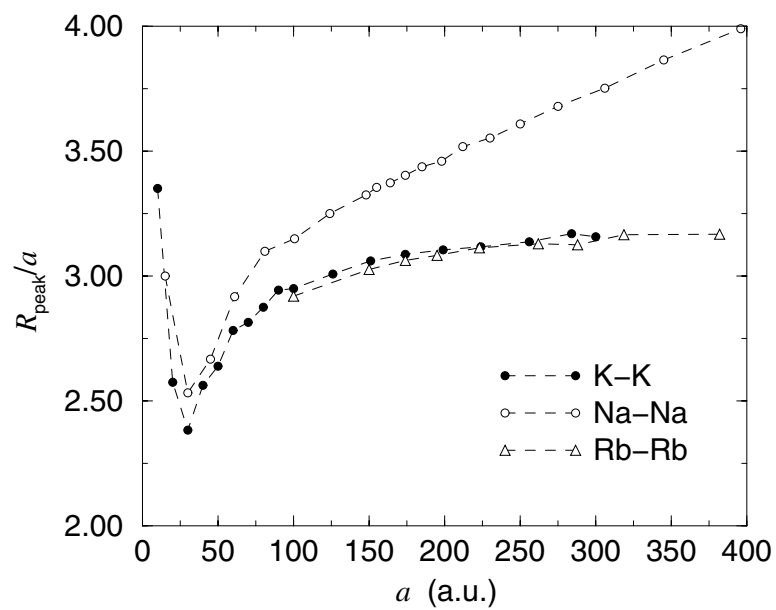


Figure 8.4: Hyperradial position of the long-range avoided crossing R_{peak} as a function of two-body scattering length a for a number of alkali potentials rescaled to support only one s -wave bound state.

into the highest s -wave dimer channel is given approximately by the expression:

$$|\mathbf{S}_{A_2+A\leftarrow A+A+A}|^2 \xrightarrow{a \rightarrow +\infty} 0.067 (ka)^4 \sin^2 \Phi, \quad (8.17)$$

where Φ is the phase difference between the amplitudes associated with the two competing pathways. An estimate of Φ can be made in the limit of large a by approximating the hyperspherical potential curve converging to the highest s -wave dimer potential as an ‘‘Efimov potential curve’’[169], i.e. $V \rightarrow -0.631/\mu R^2$, for hyperradii less than the crossing point. In this limit, the phase factor at zero energy is approximately

$$\sin^2 \Phi \xrightarrow{a \rightarrow +\infty} \sin^2 \left[\ln \left(\frac{3a}{2r_0} \right) \right], \quad (8.18)$$

where r_0 defines a characteristic length scale for the two-body potentials. (This is discussed in more detail in the caption of Fig. 8.2.) We expect that $\sin^2 \Phi$ can be approximated by $\frac{1}{2}$ in most systems having numerous two-body bound states because the amplitude of the interfering returning wave is likely to be dissipated into other recombination channels at small R . This point will require further study. However there is one atom, ${}^4\text{He}$, for which the physical two-body potentials do support only one s -wave bound state and in fact, our calculations show that the interference minimum occurs near the physical value of the scattering length. This is shown in Fig. 8.5.

Returning to Fig. 8.3, the (b) panel shows the hyperspherical potential curves, for a sech^2 two-body potential that generates a scattering length of $a = -100$ a.u., which supports a single s -wave bound state. Again, the hyperspherical potential curves are simple, but for the negative a case we find that the rate-limiting crossing occurs at small R . In fact, the hyperradius of the crossing and its coupling strength are largely independent a . The scattering length dependence of the recombination rates in the range $a < 0$ is the result of quantum mechanical tunneling under a barrier (previously identified in Ref.[169]), whose peak occurs at $R_B \approx 2a$ with a maximum height of $W(R_B) \approx \frac{0.079}{\mu a^2}$ in a.u. (see the inset of Fig. 8.3(b)). In order to reach the avoided crossing(s) at small R , the incoming wavefront in the three-body recombination channel must tunnel inside the barrier. If the incident particle does tunnel successfully, then we expect that it has a high probability to undergo a nonadiabatic Landau-Zener transition into one or more recombination channels. On the other hand, the probability per collision to tunnel into the small R region is a strong function of the barrier height and the collision energy. In fact, the probability varies as $(ka)^4$ at energies well below the barrier peak. This leads to an approximate a^4 dependence of the recombination rates for both positive and negative scattering lengths even though the recombination mechanisms are different. The existence of

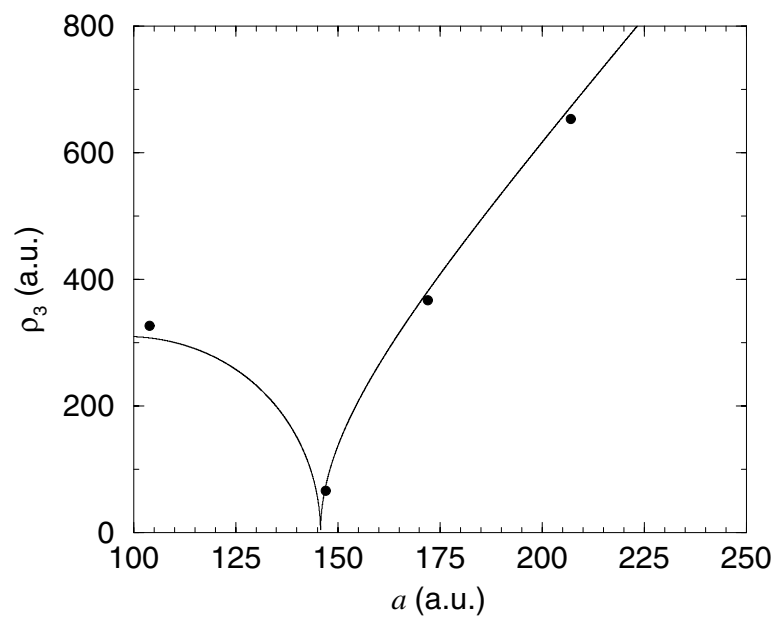


Figure 8.5: The recombination length versus scattering length a for collisions of three ${}^4\text{He}$ atoms (closed circles). The physical scattering length is $a=172$ a.u. The solid line is the analytical recombination length defined in Eq. 8.19 using $r_0=9.4$.

a potential barrier also provides the opportunity for a shape resonance in the three-body continuum to dramatically increase the recombination rates. This effect is demonstrated in Fig. 8.2 near $a \approx -175$ a.u. However, in the absence of a full calculation the positions of these resonances will be hard to predict for any real alkali system.

We have developed the following expression for the recombination length based on the roughly 125 calculations using a variety of two-body potentials:

$$\rho_3^{\text{th}}(a) \simeq \max \left\{ \begin{array}{l} \left\{ \begin{array}{l} 5.0 \left(a - \frac{3}{2}r_0\right) \left[2 \sin^2 \left(\ln \frac{3a}{2r_0}\right)\right]^{\frac{1}{4}}, a > 0 \\ -7.7a, a < 0 \end{array} \right\}, \\ 4r_0, \end{array} \right. \quad (8.19)$$

where the slopes in this expression are accurate to about $\pm 10\%$. The lower limit is set to $\rho_3 = 4r_0$ because we never see the recombination length decrease below 50-100 a.u. in the alkalis. This effect is presumably due to other recombination channels becoming more important as the dominant s -wave channel weakens sufficiently. A comparison of our analytic expression for ρ_3 with the numerically calculated $+a$ recombination lengths is shown in Fig. 8.6.

Table 8.1 provides our best estimate of the recombination rates and compares these with the available experimental information and other theoretical predictions. For the estimates of alkali rates, we have replaced the $\sin^2 \Phi$ phase factor in Eq. 8.19 with its average value of 1/2. This was not necessary for ^4He since the calculation of its recombination rate used a realistic two-body interaction potential. Table 8.1 presents the results in terms of event rates K_3 . Where necessary the quoted experimental loss rates L_3 have been converted to event rates using Eq. 8.15. In addition, the experimental results quoted for atoms in a condensate have been multiplied by a factor of 6 to compare with our theoretical results for atoms in a thermal cloud[168]. Our estimates are in reasonable agreement with most of the measured rates. The lone experiment that deviates substantially from our predicted dependence of K_3 on a is the magnetic field Feshbach resonance studied in Na[15, 172]. In particular, that experiment observed an **increase** in the recombination rate as a was **decreased** from its nominal value of $a = 54.6$ a.u. to $a = 0$. We have not observed that type of behavior in our calculations, which might suggest that the mechanism controlling the Na recombination differs from those discussed here.

The majority of the calculations performed to date used two-body potentials scaled to include only a single s -wave bound state. In order to assess the generality of our results, it is important to study the dependence of K_3 on the number of s -wave bound states, n_s , for a given a . Our preliminary results indicate that the dependence is not particularly strong. For example, the recombination event rate

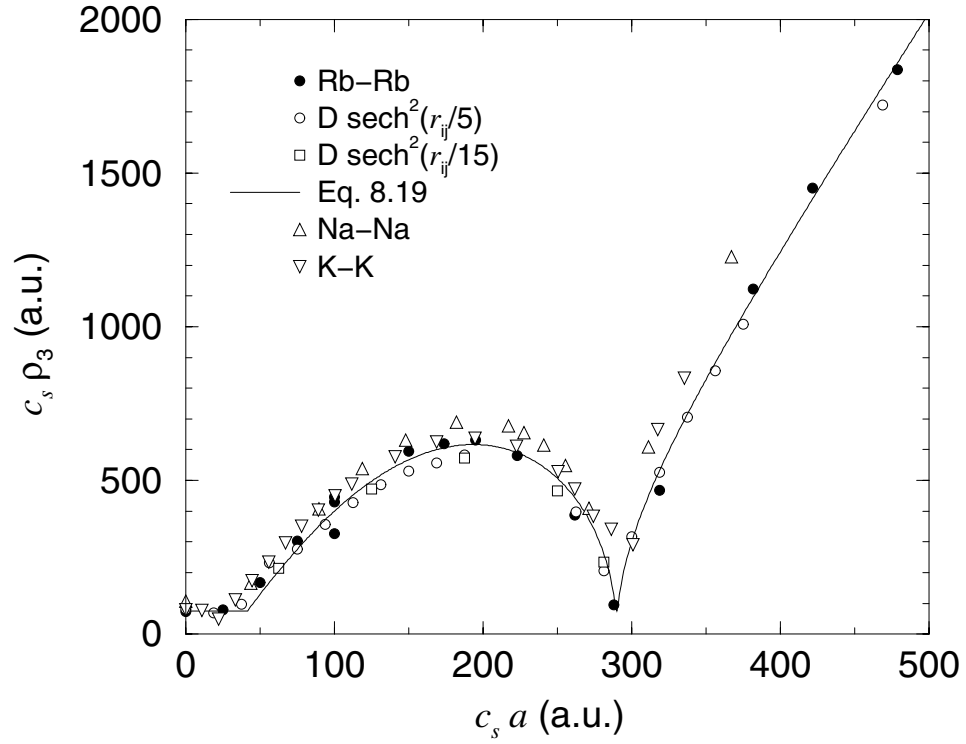


Figure 8.6: Numerical recombination lengths are compared with the $+a$ analytic formula given in Eq. 8.19 ($r_0 = 18.8$). The numerical data are discussed in the caption of Fig. 8.2.

Table 8.1: Recombination event rate constants

Atom	a (a.u.)	present K_3^{th} (cm^6/s)	experiment K_3^{exp} (cm^6/s)	other K_3^{th} (cm^6/s)
^4He	172	4.2×10^{-27}	—	2.5×10^{-27} [154]
^7Li	-27.6	2.5×10^{-28}	$< 6 \times 10^{-27}$ [173]	5.2×10^{-28} [157]
$^{23}\text{Na}(1,1)$	54.6	1.1×10^{-28}	1×10^{-27} [172]	4.0×10^{-28} [157]
^{39}K	-33	9.2×10^{-29}	—	—
^{85}Rb	-370	6.6×10^{-25}	—	—
$^{87}\text{Rb}(1,-1)$	106	2.0×10^{-28}	9×10^{-29} [168]	8×10^{-30} [157]
$^{87}\text{Rb}(2,2)$	106	2.0×10^{-28}	2.2×10^{-28} [174]	1.7×10^{-29} [154]
$^{133}\text{Cs}(3,3)$	-1250	5.6×10^{-23}	$< 10^{-23}$ [18]	1×10^{-28} [175]

K_3 was found to decrease by a factor of three when the potentials were rescaled from $n_S = 1$ to $n_S = 3$ while maintaining $a = +100$. Examining the bound state dependence of the position and strength of the rate-limiting crossing suggests that this difference will not grow much larger (see Fig. 8.7) as n_S is increased farther. The negative scattering length recombination rates have an even weaker dependence on n_S . In fact, our preliminary tests indicate that, excluding resonances, the recombination rate is essentially converged with $n_S = 1$, (see Fig. 8.8). However, these results are not conclusive and we plan to conduct more tests in the future.

It is also important to understand the energy dependence of K_3 and the energy range over which the threshold values of K_3 are applicable. For positive scattering lengths, we find that K_3 is reasonably constant over collision energies ranging from $E = 0$ to several hundred μK . However, owing to the low energy barrier in the entrance channel, K_3 is far more energy-dependent for the negative scattering lengths. In fact, the threshold limit for K_3 is achieved at $a < 0$ only for collision energies well below the barrier maximum. At higher energies, the scattering probability saturates and K_3 decreases due to the k^{-4} factor (see equations 8.13 and 8.14). The energy dependence of the recombination rates for $\pm a$ are shown in Fig. 8.9. This behavior should have a dramatic effect on the ^{133}Cs recombination rates if $a \approx -1250$ as quoted in Ref.[18]. In this case, the peak of the barrier in the three-body entrance channel is roughly $W(R_B) = 0.1\mu\text{K}$. Our experience suggests that K_3 will decrease several orders of magnitude as the collision energy rises to $10\mu\text{K}$. The resulting rate would then be consistent with the experimental bound set in Ref.[18] even though our threshold value is greater than the bound quoted in Ref.[18](see Table 8.1).

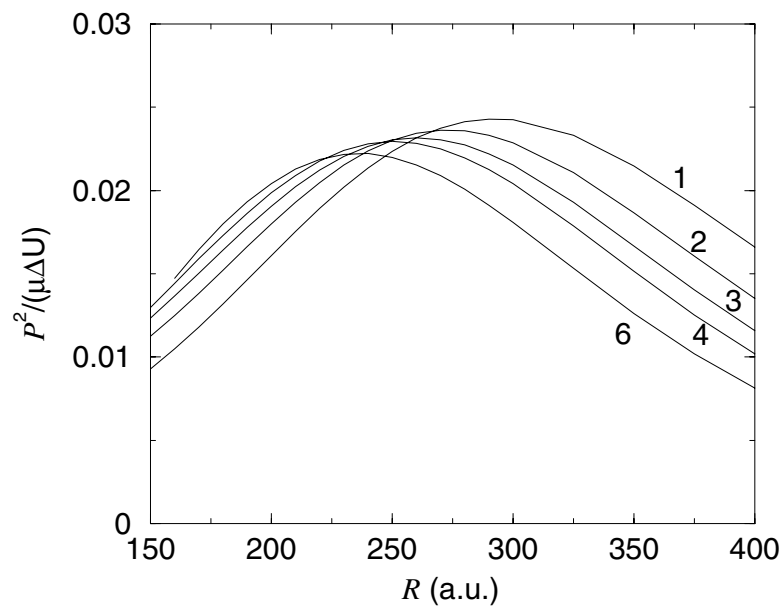


Figure 8.7: Coupling between the three-body entrance channel and the highest s -wave recombination channel is shown as a function of hyperradius. Each curve represents a Rb-Rb potential rescaled to hold n_S s -wave bound states with $a=+100$. The labels on each curve denote the number n_S .

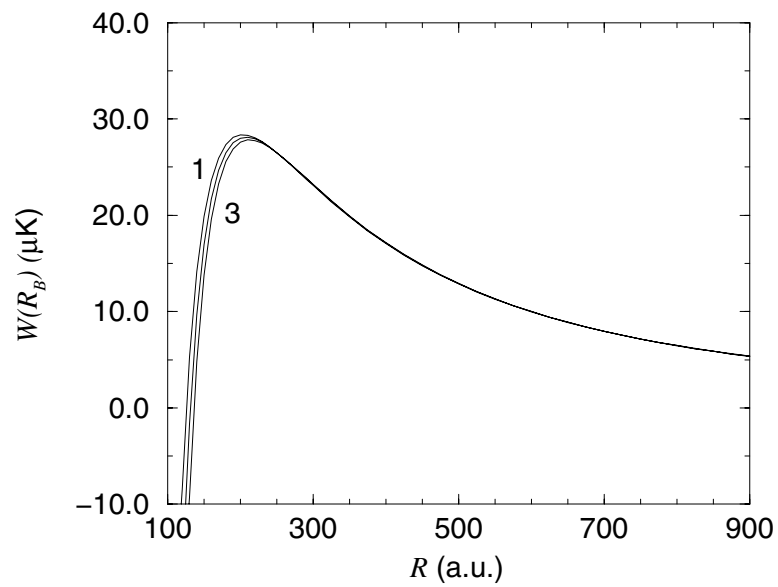


Figure 8.8: The centrifugal barrier in the three-body entrance channel is shown as a function of hyperradius. Each curve represents a Rb-Rb potential rescaled to hold n_S s -wave bound states with $a = -100$ a.u. Curves with $n_S = 1$ and 3 are labeled, $n_S = 2$ is the unlabeled curve. The height and position of the barrier are essentially independent of n_S . The event rates K_3 calculated for these three potentials varied by roughly 30%.

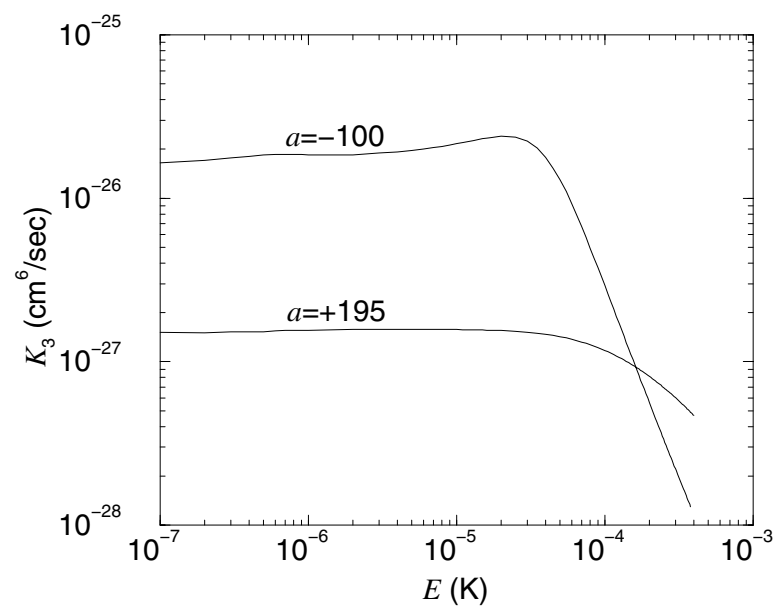


Figure 8.9: The energy dependence of K_3 is shown for $\pm a$. These data used Rb-Rb potentials rescaled to support one s -wave bound state. The negative scattering length recombination rate exhibits an E^{-2} dependence for collision energies above the barrier in the three-body entrance channel ($W(R_B) \approx 30\mu\text{K}$ for this example).